Carbon xxx (xxxx) 1–9

Contents lists available at ScienceDirect

Carbon

journal homepage: www.elsevier.com/locate/carbon

Research Article

Highly sensitive broadband binary photoresponse in gateless epitaxial graphene on 4H–SiC

Shivi Rathore [a], Dinesh Kumar Patel [b, c], Mukesh Kumar Thakur [d], Golam Haider [d, **], Martin Kalbac [d], Mattias Kruskopf [e], Chieh-I Liu [c, f], Albert F. Rigosi [c], Randolph E. Elmquist [c], Chi-Te Liang [b, ***], Po-Da Hong [a, *]

[a] Department of Materials Science and Engineering, National Taiwan University of Science and Technology, Taipei, 106335, Taiwan
[b] Department of Physics, National Taiwan University, Taipei, 106319, Taiwan
[c] Physical Measurement Laboratory, National Institute of Standards and Technology (NIST), Gaithersburg, MD, 20899, USA
[d] J. Heyrovsky Institute of Physical Chemistry, Czech Academy of Sciences, Prague 8, Czech Republic
[e] Physikalisch-Technische Bundesanstalt (PTB), Bundesallee 100, D-38116, Braunschweig, Germany
[f] Department of Chemistry and Biochemistry, University of Maryland, College Park, MD, 20742, USA

ARTICLE INFO

Article history:
Received 7 June 2021
Received in revised form 20 July 2021
Accepted 30 July 2021

Keywords:
Silicon carbide
Epitaxial graphene
Broadband photodetector
Binary response

ABSTRACT

Due to weak light-matter interaction, standard chemical vapor deposition (CVD)/exfoliated single-layer graphene-based photodetectors show low photoresponsivity (on the order of mA/W). However, epitaxial graphene (EG) offers a more viable approach for obtaining devices with good photoresponsivity. EG on 4H–SiC also hosts an interfacial buffer layer (IBL), which is the source of electron carriers applicable to quantum optoelectronic devices. We utilize these properties to demonstrate a gate-free, planar EG/4H–SiC-based device that enables us to observe the positive photoresponse for (405–532) nm and negative photoresponse for (632–980) nm laser excitation. The broadband binary photoresponse mainly originates from the energy band alignment of the IBL/EG interface and the highly sensitive work function of the EG. We find that the photoresponsivity of the device is > 10 A/W under 405 nm of power density 7.96 mW/cm^2 at 1 V applied bias, which is three orders of magnitude greater than the obtained values of CVD/exfoliated graphene and higher than the required value for practical applications. These results path the way for selective light-triggered logic devices based on EG and can open a new window for broadband photodetection.

1. Introduction

Recently, graphene has attracted much attention in the area of optoelectronic devices due to its high carrier mobility, optical transparency, mechanical flexibility, strength, and thermal stability [1–8]. Ultrafast and broadband absorption make graphene an ideal candidate for broadband photodetectors [9,10], which are crucial for next-generation optoelectronic applications in national defence, biological imaging, chemical sensors, displays, and spectroscopy [2,3,11–17]. In particular, designing a binary photoresponse device based on graphene alone would be highly beneficial for optical signal processing and logic device applications [18]. However, exfoliated pristine and chemical vapor deposition (CVD) monolayer graphene yield photodetector devices that suffer from low-photoresponsivity [19–22] due to weak optical absorption [9] and ultrafast recombination photogenerated carriers in the graphene layer before getting separated by the electric field [23,24]. Therefore, developing a better-performing graphene-based binary photodetector is highly desired. Wide-bandgap silicon carbide (SiC)- and GaN-based solid-state photodetectors are popular due to their reliability and lightweight. Specifically, epitaxial graphene (EG) on SiC could be an alternative choice for these practical optoelectronic applications due to its high breakdown fields, inherent bandgap induced by the underpinning interfacial buffer layer (IBL), and its metrology-grade quality [25–32].

Previous reports on SiC-based photodetectors include single photoresponses either in the ultraviolet (UV) or visible region [33–37]. Recently, non-local photodetection in graphene [38] and substrate-induced photofield effects in EG Refs. [39,40] have been reported. CVD graphene on SiC has been shown to possess a hysteretic response to photoexcitation [41], and asymmetric metal-EG interfaces are reported

* Corresponding author.
** Corresponding author.
*** Corresponding author.
E-mail addresses: haider.golam@jh-inst.cas.cz (G. Haider), ctliang@phys.ntu.edu.tw (C.-T. Liang), poda@mail.ntust.edu.tw (P.-D. Hong).

https://doi.org/10.1016/j.carbon.2021.07.098
0008-6223/

to have a tunable response to the excitation across the junction [42,43]. Li et al. reported the binary photoresponse at the planner *n-n-n* junction in an EG film [44]. These photodetector devices require high electrostatic potentials and light exposure simultaneously. The photoresponsivity quickly falls off to zero when the electrostatic potential approaches zero. In many sensing applications, top or back gating is not always feasible due to complicated structures. To overcome this problem, it is important to develop a gate-free, EG/4H–SiC-based photodetector that can operate even in the broadband region. However, the role of IBL layer for photodetection is not clearly understood. Thus, fabrication and characterization of EG/4H–SiC-based devices will be beneficial for understanding charge transfer through different constituent layers [45–47] and magneto-transport experiments [45,46].

In this work, we demonstrate electrostatic gate-free, broadband, and binary photoresponses in EG/4H–SiC-based devices having the simplest device design. We use as-grown bare monolayer EG on a 4H–SiC substrate to fabricate our devices. We report both positive and negative photoresponse observations without the assistance of electrostatic gating under the illumination of the different wavelengths of laser light. Additionally, our devices responded strongly to excitation wavelengths ranging from 405 nm to 980 nm, yielding responsivities higher than 10 A/W under 405 nm of power 7.96 mW/cm^2, which is three orders of magnitude higher than those based on CVD and exfoliated graphene. This unusual phenomenon motivates us to study the photodetection in EG/4H–SiC-based devices as well as to test the role of IBL in the photodetection process. Further confirmation of the photodetection mechanism is provided by carefully studying two different control devices without the IBL on the similar SiC substrate: (1) a thin layer of exfoliated graphene with pre-fabricated electrodes on only bare SiC to see the effects of the IBL and metal contacts, (2) a dummy device with two electrodes on only SiC to understand the role of the substrate.

2. Experimental details

The detailed growth process of high-quality epitaxial graphene can be found in Refs. [47,48]. EG is formed when Si atoms sublimate from the silicon face of SiC. Samples were grown on square SiC chips 7 × 7 mm^2 to 21 × 21 mm^2 diced from on-axis 4H–SiC (0001) semi-insulating wafers (CREE). Chips were first cleaned by ultrasonication in acetone and isopropanol (IPA) followed by hydrofluoric (HF) acid and processed with AZ5214E for polymer-assisted sublimation growth (PASG) [49]. The face-down configuration [50] in combination with PASG promotes homogeneous growth [47]. The high-temperature annealing process was performed in an ambient argon environment at 1850 °C for 240 s–300 s with a graphite-lined resistive-element furnace (Materials Research Furnaces Inc). The heating and cooling rates were about 1.5 °C/s. Note that in the thermal decomposition of SiC at high temperatures in an argon atmosphere, Si atoms sublimate and carbon atoms nucleate and reconstruct into amorphous interlayer $(6\sqrt{3} \times 6\sqrt{3})$R30 structure, with the decomposition process allowing IBL to change into graphene while forming a new IBL between the EG film and SiC substrate. About one-third of the carbon atoms in the IBL are covalently bound to the (0001) face of the SiC substrate. The interaction of remaining silicon bonds from the SiC surface, with the graphene layer influences the electronic transport properties. This, together with the orbitals of graphene and SiC overlapping, produces the intrinsic *n*-type doping in EG [51,52].

After evaluation and characterization of successfully grown EG with Raman spectroscopy and atomic force microscopy (AFM), we deposited a thin protective layer of Pd and Au (10 nm/15 nm respectively), using a Denton Vacuum Infinity 22 e-beam evaporator on the EG to prevent organic contamination. Then we spin coat lift-off resist (LOR) 3A for the undercut and then S1813 photoresist at 6000 rpm each, followed by standard baking procedures of each photoresist. Next, we wrote the graphene structure using a Heidelberg maskless aligner (MLA150) and developed samples in MF26A for 1 min, followed by a wash with deionized (DI) water. Once the pattern developed nicely, again we deposited a gold layer (80 nm) as a metal mask followed by lift-off in PG remover at 80 °C for 30 min and washed it with DI water and IPA. After that, EG is etched at room temperature into the desired device shape with 40 sccm Ar/O_2 plasma using the Unaxis 790 Reactive Ion Etcher (RIE) tool for 7 min using a pressure of 4 Pa, 100 W power, and 300 V DC voltage. Once the graphene pattern is in the desired shape, we follow the same recipe to spin coat LOR 3A, Shipley S1813, and develop after UV exposure for the Au base contact electrodes. Next, we deposited niobium titanium nitrate (NbTiN) for electrodes using a Denton Vacuum Discovery 550 sputtering tool followed by lift-off in PG remover. Finally, we remove the protective layers from the EG region using a solution of 1:1 aqua regia to deionized water [53,54].

For the thin layer of exfoliated graphene device and transfer technique, please see our previous work [55]. In short, we used natural kish graphite from Graphene Supermarket to fabricate the exfoliated graphene device on a similar SiC substrate. In order to maintain the exfoliated graphene film quality, we mechanically exfoliate the thin layer of graphene onto a polydimethylsiloxane stamp. Then we dry-transfer graphene onto pre-patterned electrodes on the SiC substrate by the viscoelastic method without any polymer films attached to our flakes.

The Raman spectra were measured with a WITec alpha300 R spectrometer equipped with a piezo stage. The excitation laser wavelength 532 nm and the laser power 1 mW were used. The laser was focused on the sample with a 100 × objective to a spot with a diameter of around 500 nm. Asylum Cypher high-resolution AFM was used to image the SiC terraces and EG growth quality at the atomic level. UV–visible spectra were measured with a UV/Vis/NIR spectrometer (PerkinElmer Lambda 1050). The current-voltage measurements were done using a Keithley 2400 source meter.

3. Results and discussion

Raman spectroscopy is one of the most efficient techniques to study the doping, strain, quality with respect to defects, and layer number of graphene, in general. The Raman spectra of EG/4H–SiC are shown in Fig. 1(a) without background subtraction, where all the important peaks can be observed and are marked. Here, we observe a symmetric 2D peak at about (2716.6 ± 0.8) cm^{-1} and a graphene G peak at around (1604.5 ± 0.6) cm^{-1}, including SiC peaks around at 1524 and 1718 cm^{-1} which are consistent with previous reports [56,57]. The insignificant magnitude of the defect-associated D peak at around (1384.5 ± 8.9) cm^{-1} suggests that EG is nearly defect-free. Additionally, the Raman spectra show characteristics of monolayer EG on 4H–SiC (0001) with an FWHM of (41.5 ± 1.8) cm^{-1} and a peak position of (2716.6 ± 0.8) cm^{-1}, produced using the combined methods of face-to-graphite and PASG as inhibitors of growth [49]. We used an Asylum Cypher high-resolution AFM to image the terraces in the SiC substrate at the nanoscale level. Fig. 1(b) shows an AFM image of a typical uniform terrace structure of monolayer EG over the substrate. The Si face to graphite technique and PASG allow exceptionally low steps ≤1 nm over a large scale (see inset of Fig. 1(b)). The uniformity in trace and nm scale step height indicate that graphene is uniform and of high quality for optoelectronic applications with minimum resistance anisotropy.

After evaluating and characterizing grown EG with Raman and AFM, a photolithography process (see Fig. 1 (c)) was implemented to fabricate all devices, including steps for NbTiN contacts [53,54]. The devices are imaged by a confocal microscope [58]. Fig. 1 (d) is a magnified image of our Hall bar device. Small bilayer EG regions (as indicated by an arrow) form along with the step-edge facets because the edges of many SiC (0001) atomic layers are exposed through step bunching. No extended regions of the bilayer are observed. The potential reasons for the negative impact of step edges are variations of the doping level,

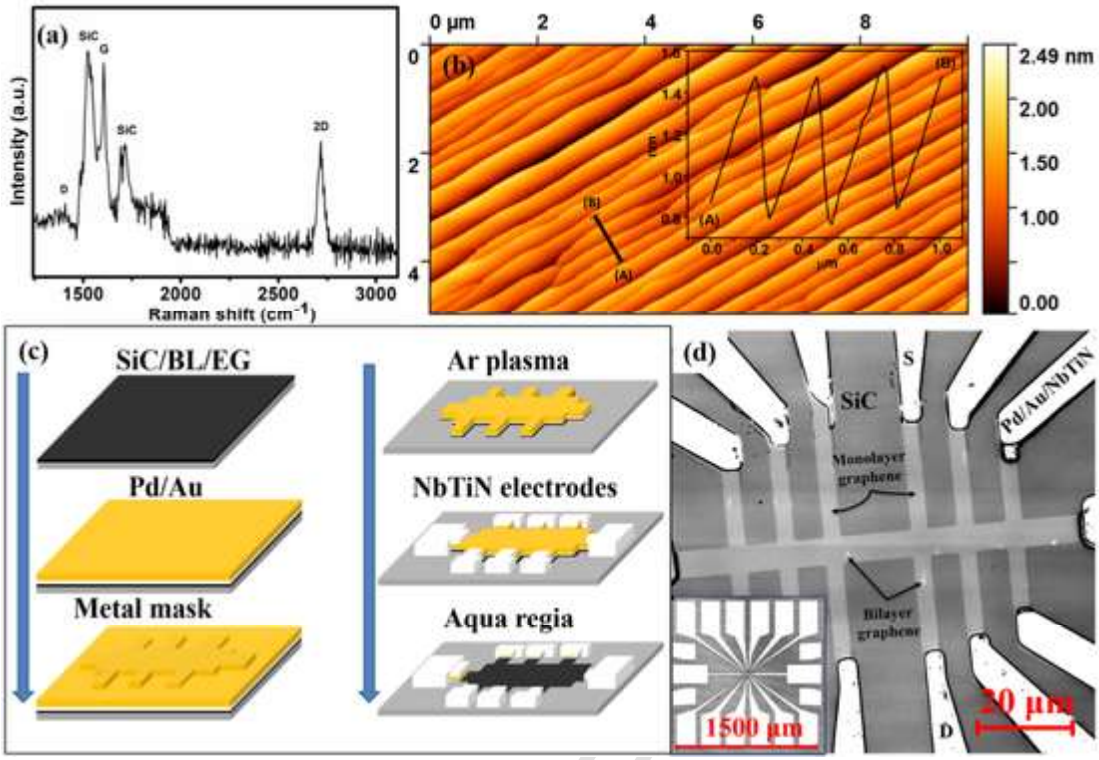

Fig. 1. Fabrication and optical characterization of the device. (a) Raman spectrum of the EG/4H–SiC showing 2D, G and D peak around (2716.6 ± 0.8) cm^{-1}, (1604.5 ± 0.6) cm^{-1} and (1384.5 ± 8.9) cm^{-1}, respectively including SiC peaks around 1524 cm^{-1} and 1718 cm^{-1}. (b) The AFM image shows the uniform surface morphology of the EG on the SiC substrate. The inset shows the height profile with typical terrace step heights of about 1 nm. (c) Schematic of the residue-free device fabrication process. After the EG growth on SiC, a thin layer of palladium and gold is deposited to protect the film. Photolithography and sputtering were then used to complete the device. Finally, the protective metals are etched from EG with diluted aqua regia. (d) The confocal microscopy image of the EG/4H–SiC-based device is shown. The image highlights the homogeneity of the EG film, showing a few small patches containing bilayers, as indicated by arrows. Inset is the confocal image of a complete device in which fourteen NbTiN electrodes are connected to the EG. (A colour version of this figure can be viewed online.)

scattering centers, and strain due to a local detachment of the EG layer at the edges of the terrace of the substrate. Fabricating Hall bar enables us to host an array of photodetectors, allows simultaneously determining the carrier density and mobility *via* different modes of transport measurement with and without magnetic field *B*.

We used an Oxford Triton 200 dilution refrigerator system in our previous low-temperature magneto-transport measurements on the devices [55] to determine the carrier density (n) and mobility (μ). The formulas $n = \frac{1}{e\left(\frac{dR_{xy}}{dB}\right)}$ and $\mu = \frac{1}{en\rho_{xx}}$ were used to determine the carrier density and mobility of EG/4H–SiC-based device at 100 mK. Here e is the elementary charge, B is the applied magnetic field perpendicular to the graphene plane, and R_{xy} is the Hall resistance. The carrier density and mobility of EG/4H–SiC-based device are found to be about 1.58×10^{12} cm^{-2} and 2350 cm^2 V^{-1} s^{-1}, respectively [55], and which provide a signature of high-quality *n*-type doped graphene.

The optoelectronic characterizations of the device were performed using a Keithley 2400 source meter and under the excitation of laser photons of different flux densities and energies at ambient conditions without any focusing lenses. The current-voltage (*I–V*) characteristics of the heterojunction device were studied under the different illumination and power density of (405, 532, 640, 808, and 980) nm laser excitation, as shown in Electronic Supporting Information (ESI) (Fig. S1). The corresponding photocurrent-voltage plots are shown in Fig. 2, where photocurrent, *viz.* photo-source-drain-current, is defined as, $\Delta I_{SD} = |(I_{light} - I_{dark})|$.

The *I–V* characteristics of the device shown in Fig. 2 and Fig. S1 are linear, consistent with the previous reports of graphene-based field-effect transistors on arbitrary substrates [37,42]. Interestingly, we found that the obtained device current possesses different polarities under the illumination of different excitations, shown by the arrows in ESI Fig. S1. For the higher energy excitations 405, and 532 nm, as shown in Fig. 2 (a) and (b), positive photoresponses and, for the lower energy excitations 633–980 nm, Fig. 2 (c – f), shows negative photoresponses were observed. Additionally, it is found that the photocurrent for the 405 nm excitation is much higher and gradually decreases with incident photon energy.

To demonstrate photodetection, we studied photo-switching of the device current under periodic illumination of different light sources. The dynamic photo-source-drain current studied under the illumination of the same photon flux of ~79.6 mW/cm^2 for different lasers of wavelength from 405 nm to 980 nm at a bias voltage of V_{DS} = 1 V is shown in Fig. 3(b).

As observed in the *I–V* characteristics, the dynamic photocurrent also possesses the following two properties: (i) under the higher energy excitation (405 and 532 nm), the photoresponse is positive (see Fig. 3 (b)). (ii) For 632–980 nm, negative photoresponses were observed, and the photocurrent gradually decreased with excitation energy, as shown in Fig. 3 (b). We repeatedly measured the device over an extended period under different powers to demonstrate the stability and reproducibility of the observation, as shown in the ESI (Fig. S2). The photocurrent at low energy excitation shows saturation behaviour, while the photocurrent at higher energy excitation with a similar light on/off frequency remains unsaturated. To obtain a saturated photocurrent under the higher energy excitation, we illuminated the devices with an extended period, as shown in ESI (Fig. S3).

The broadband binary photoresponse of the EG/4H–SiC-based device can be explained in terms of absorption in both the IBL and EG as well as the photogenerated charge transfer between them. To further understand the role of the IBL, we have also studied devices with just

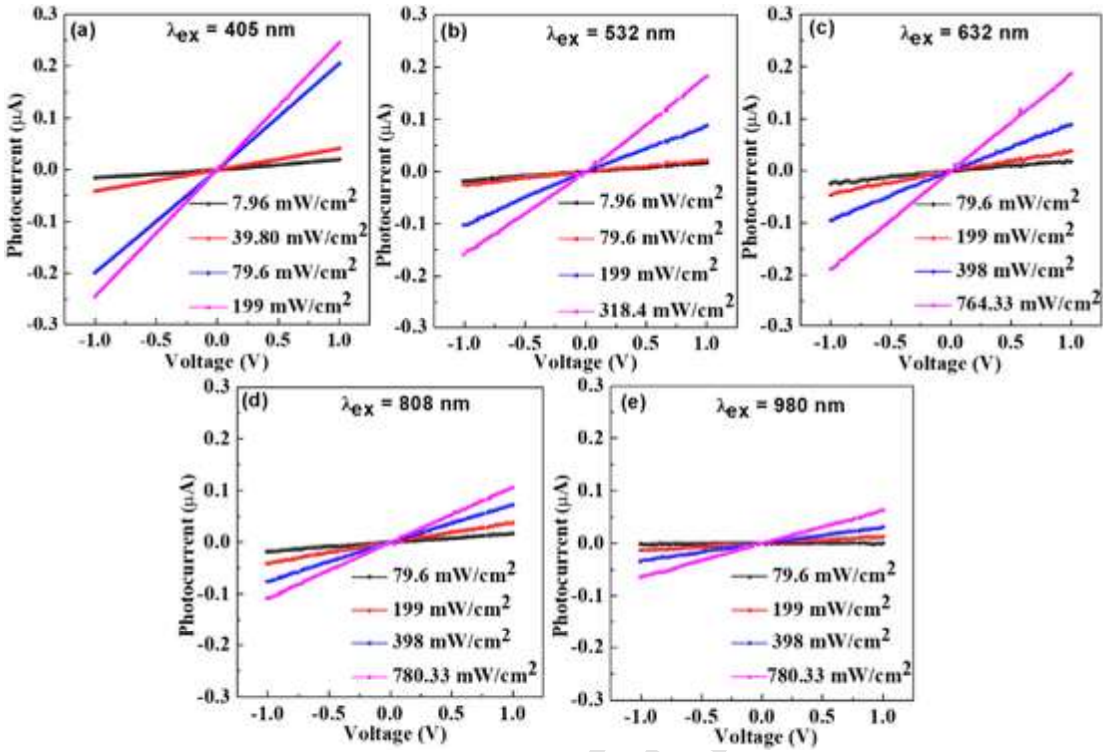

Fig. 2. Absolute photocurrent *vs.* voltage characteristics of the EG/4H–SiC based device under different power densities of (a) 405, (b) 532, (c) 633, (d) 808, and (e) 980 nm laser excitations, obtained from *I–V* characteristics shown in Fig. S1. The values of the power densities are mentioned in each panel. (A colour version of this figure can be viewed online.)

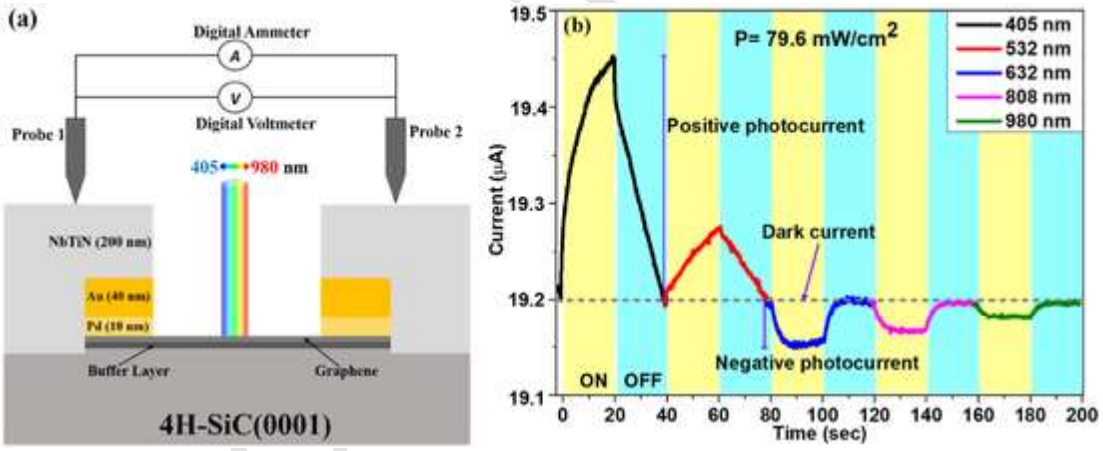

Fig. 3. (a) Schematic illustration of the EG/4H–SiC-based device and two-probe photodetector measurement setup with IBL under EG. (b) The dynamic photoresponse of the EG/4H–SiC-based device under 405, 532, 632, 808, and 980 nm excitation of intensity 79.6 mW/cm^2 at V_{DS} = 1 V. The switching behaviour of the device is marked as ON (light yellow) and OFF (light blue). (A colour version of this figure can be viewed online.)

SiC (substrate) and a thin layer of exfoliated graphene on SiC (without IBL), both of which show a negligible photoresponse compared to the EG/4H–SiC-based device (see ESI Figs. S4 and S5). According to these observations, it is clear that the IBL plays a significant role in photodetection in EG/4H–SiC-based devices. Recent investigations of the optoelectronic properties of IBL reveal that it exhibits a bandgap due to structural imperfections (thickness nonuniformity, ripples, domains with different doping levels, *etc.*) that appear during EG formation [25–31]. Therefore, it could be expected that the IBL plays a critical role in the broadband absorption spectra due to the absorption at different electronic levels. Combined with the EG layer contribution to the broadband absorption, the reported observations of the excitation energy-dependent IBL binary photoresponse behaviours appear reasonable but still require clarification.

To understand the observed broadband binary photoresponse more clearly, the energy band diagram of the device is drawn in Fig. 4 under different laser illumination [59–62]. It is reported that the IBL in the EG/4H–SiC-based system possesses a variable bandgap between the wide-bandgap 4H–SiC of 3.2 eV due to the graphene-substrate interaction induced bandgap and sublattice symmetry breaking (about 0.2 eV) [25–31]. Additionally, such layer accommodates massive deep-level trap centers, which efficiently *n*-dope the EG layer [31]. As a result, a built-in electric field (E_b) is generated in thermal equilibrium at the IBL/EG interface. This causes an upward band bending at the interface that assists the migration of photogenerated charges at the interface (Fig. 4 (a)). For laser excitation from 632 to 980 nm, the photocurrent is dominated by the absorption in the graphene layer. This is due to the fact that such low-energy excitations are incapable of efficient genera-

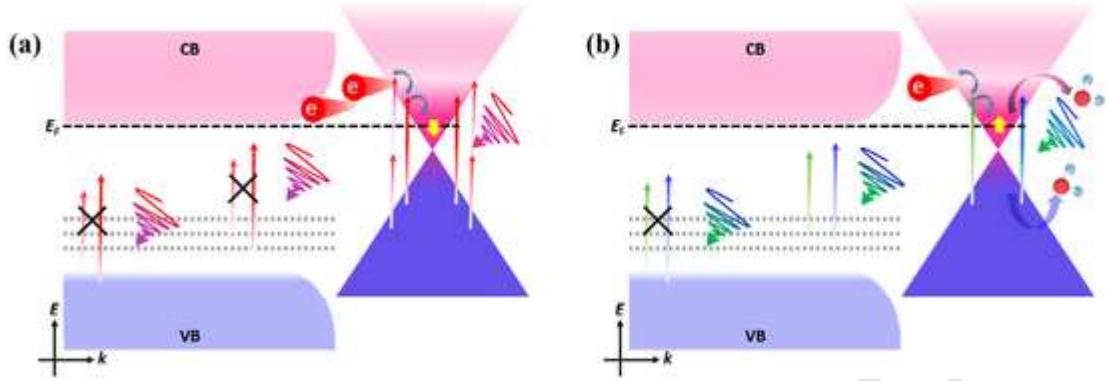

Fig. 4. The schematic illustration of the energy band diagram of the EG/4H–SiC-based system showing the photocurrent generation process for the excitation of 632 nm and larger (a), as well as 532 nm and lower wavelengths (b). VB and CB represent the valence and conduction band of SiC, the dotted lines between *VB* and CB resemble the deep defect levels of IBL, E_F is the Fermi energy of the system. (A colour version of this figure can be viewed online.)

tion of photocarriers both from the valence band (VB) of SiC and the deep defect levels of the IBL. Owing to the presence of E_b, the photogenerated electrons from the EG transfer to the SiC layer on a time scale of 0.3 fs, leaving photogenerated holes in the graphene layer [63]. As a result, the Fermi energy of the graphene layer reduces, which causes the lowering of the device current, as shown in Fig. 3 (b). The stark contrast between the photoresponses for 532 nm and that for 405 nm can be understood when considering the wide bandgap, wherein an excitation for SiC is not possible. The defects in the IBL can enhance the intrinsic absorption in monolayer EG, which results in reduction of negative charges in the EG layer. However, it is known that in ambient conditions, physisorbed gas molecules [64] in single layer graphene efficiently release from the layer under those high energy excitations, which as a result increases the *n* doping in the EG layer, see Fig. 4(b) [59,65–67] and a positive photocurrent. Note that releasing such adsorbed gases is much slower than the interlayer charge transfer time scale [59,67]. Thus, the transient photocurrent response is found to be slower. More explicitly, as shown in Fig. 4(b), the photoabsorption at the layers cause electron deficiency due to the electron transfer from graphene to IBL. However, the release of ambient gas molecules causes *n* doping to the graphene layer, which surplus the electron deficiency due to photon absorption. This competition and slow release of adsorbates cause a slower change of the device current [68]. On the other hand, the release of ambient gas molecules in lower-energy excitation is not significant [69–71]. Additionally, the photoinduced interfacial charge transfer process in the EG-IBL interface due to the lower energy excitations is an ultrafast phenomenon [63], which results in a faster response. In our recent study on ZnO-graphene-based phototransistors, we demonstrated that application of gate voltage significantly influences the photoinduced adsorption/release processes; and a rapid saturation is achieved by applying a negative gate voltage [67]. No such external electric field is applied here; thus, the process remained slow. The dynamic photocurrent for higher energy excitations (405–532 nm) can be expressed as, $\Delta I_{SD} = \Delta I_{Ph}\left\{1 - \exp\left(-\frac{t}{\tau_r}\right)\right\}$, where, $\Delta I_{Ph}$is the saturated photocurrent of the device, τ_r is the response time. Similarly, for low energy excitations (633–980 nm), the dynamic photocurrent can be expressed as, $\Delta I_{SD} = \Delta I_{Ph}\left\{\exp\left(-\frac{t}{\tau_r}\right) - 1\right\}$ [59,67]. Thus, the magnitude of the obtained photocurrent, $\Delta I_{SD}$is dependent on the repetition rate of the incident laser pulses. When the frequency is higher than the characteristic frequency of the device ($1/\tau_r$), an unsaturated photocurrent is obtained, which results in an underestimated device performance [72]. We expect that, for measurements under vacuum, after the arrival of first few higher energy pulses, the photocurrent will switch its polarity, and it is expected to show a negative photoresponse for all of the excitation energies. The scenario will be different under the controlled environment of different gases [71].

The responsivity *R* is an important parameter to assess the photodetection ability of the device, and it is defined as the photocurrent generated per unit power of the incident light [73] and can be written as

$$R = \frac{|\Delta I\,(A)|}{P\,(W)}, \tag{1}$$

where $|\Delta I|$ is the absolute photocurrent measured in amperes (A), and *P* is the incident light power on the active device area measured in watts (W). The wavelength-dependent photoresponsivity of the device is shown in Fig. 5 (a), where the maximum responsivity was observed for 405 nm excitation, which agrees well with previous work [36]. The EG/4H–SiC-based device has higher absorption in the high energy region; thus, the obtained behaviour of photoresponsivity is consistent with the absorption profile of the composite, as shown in Fig. 5 (a). The highest value of the photoresponsivity is found to be 10 A/W for the 405 nm excitation and 1.7 A/W for the 532 nm excitation at a power density of 7.96 mW/cm^2 and applied bias of 1 V. Responsivity as a function of incident power density is shown in Fig. 5 (b) for 405 nm excitation. With the gradual enhancement of power, the photoresponsivity is found to decrease exponentially. The decrease results from the photocurrent not scaling with the incident power due to saturable absorption of graphene, filling of trap states, *etc.*, consistent with previous reports [59,67]. The responsivity of the devices under different laser excitations at a constant power density of about 79.6 mW/cm^2 has been tabulated in Table 1.

The photocurrent gain (Γ_n) of the device can be defined as,

$$\Gamma = \frac{h\nu}{P}\frac{|\Delta I|}{\eta e}, \tag{2}$$

where $_h\nu$ is the photon energy (1240.59/λ (nm)), $|\Delta I|$ is the absolute photocurrent, *e* is the elementary charge, *P* is the incident power, and η is the quantum efficiency for carrier generation per absorbed photon. For simplicity, we assumed $\eta = 1$ to underestimate the Γ_n value. Fig. 5 (c) shows the spectral variation of gain (Γ), which has a similar variation with *R* and is nearly identical to the absorption profile of the system for lower energy excitations. The strong deviation of the *R* and Γ profile from the absorption spectrum at higher energy is due to the involvement of the physisorbed molecule in the graphene layer, which makes the photocurrent higher.

The specific detectivity D^* is another key parameter to characterize the sensitivity of the photodetector. The Jones unit is defined to be 10^{-2} m Hz$^{1/2}$ W^{-1}. D^* is expressed by the following equation:

$$D^* = \frac{R\sqrt{a}}{\sqrt{2eI_d}}, \tag{3}$$

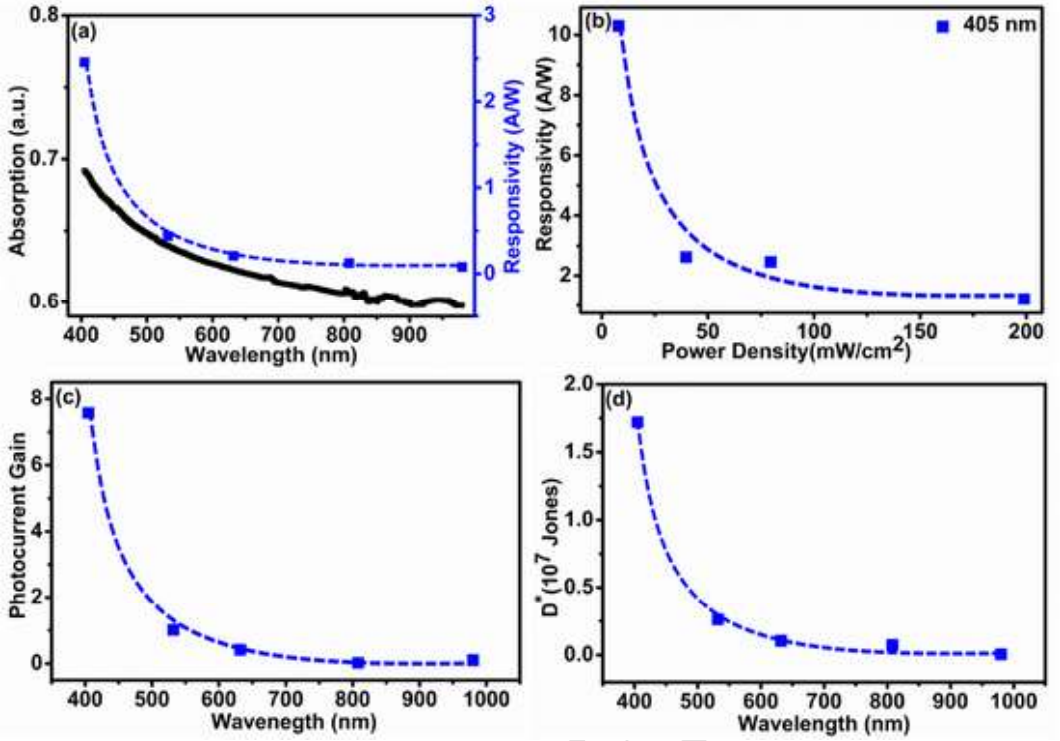

Fig. 5. All measurements were done at V_{DS} = 1 V, and at power density 79.6 mW/cm^2. (a) The wavelength-dependent responsivity (right axis) and absorption (left axis) are shown. (b) The power density-dependent photoresponsivity of the EG/4H–SiC-based devices for 405 nm. (c) and (d) are the gain and detectivity of the EG/4H–SiC-based devices, respectively. The lines joining the data points are a guide to the eye only. The Jones unit is defined to be 10^{-2} m Hz$^{1/2}$ W^{-1}. (A colour version of this figure can be viewed online.)

Table 1
Photoresponse characteristic parameters of our EG/4H–SiC-based device under different illumination wavelengths at fixed applied voltage and power density.

Wavelength (nm)	Responsivity (A/W) (@V_{DS} = 1V, 79.61 mW/cm^2)	Gain (@V_{DS} = 1V, 79.61 mW/cm^2)	Detectivity (x10^7 Jones) (@V_{DS} = 1V, 79.61 mW/cm^2)	Response time (τ_{rise}) (s)	Recovery time (τ_{rise}) (s)
405	2.457	7.57	1.72	17.37	15.61
532	0.437	1.01	0.261	15.25	13.68
632	0.209	0.409	0.01	6.60	2.30
808	0.123	0.188	0.073	7.69	5.64
980	0.078	0.098	0.0044	5.40	4.50

where R is the responsivity, 'a' is the active area of the device, e is the elementary charge and I_d is the dark current. The highest D^* for the device was found at 1.7 × 10^7 Jones for the 405 nm excitation at 79.6 mW/cm^2 and V_{DS} = 1 V (see Fig. 5 (d)).

The response time is another key parameter of a photodetector device. The response (τ_{rise}) and recovery (τ_{fall}) time of the devices are defined as the time difference between 10% and 90% of the peak value of the photocurrent during the photoexcitation and dark (off) side, respectively [74]. Fig. 6 (a) shows the response time for the 405 nm laser excitation (positive photoresponse) with τ_{rise} and τ_{fall} nearly 17 s and 16 s respectively, whereas, in the case of 980 nm (negative photoresponse), the τ_{rise} and τ_{fall} are around 5 s (see Fig. 6 (b)). Fig. 6 (c) shows the wavelength-dependent response and recovery time under the exposure of photons of constant power density, which is consistent with the pro-

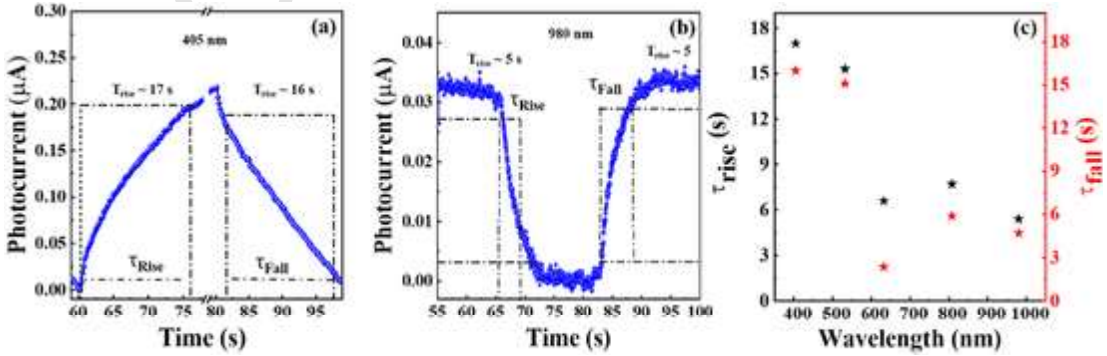

Fig. 6. Response time for (a) 405 nm, and (b) 980 nm excitation. (c) Wavelength-dependent response time (left axis) and recovery time (left axis) are shown at V_{DS} = 1 V and at 79.6 mW/cm^2 power density. (A colour version of this figure can be viewed online.)

posed underlying mechanism. Table 1 compiles the calculated parameters of photodetector at fixed biased voltage 1 V, at 79.6 mW/cm^2 power density with different wavelengths of the laser source. Note that these response times are higher than those of the other EG/4H–SiC-based devices [35,38,44] because our device lacks an electrostatic gate. We propose that the high photoresponsivity at a lower bias voltage is a result that requires further investigation.

To further support the observed broadband binary photoresponse behaviour in our devices, we additionally investigated multiple devices with different geometry and graphene growth run. Three data sets (devices 23, 27, and 32 correspond to those produce at R 311 run) are shown in Fig. S6. All EG/4H–SiC-based devices show the same behaviour. The observation remains unchanged with the devices that contain different layer numbers, as shown in Fig. S6. We summarized all the devices' photoresponse behaviour in Table S1. All devices exhibit broadband binary photoresponses without electrostatic gating, demonstrating the robustness of this phenomenon in our EG/4H–SiC-based devices.

Furthermore, we compared the photodetector parameters to those of other EG on SiC-based devices, including hydrogen intercalated, CVD, and exfoliated graphene/SiC-based photodetectors [36–38,41,44,75,76] as shown in Table 2. Our EG/4H–SiC-based devices showed a broadband binary response with high responsivity without an applied gate voltage, dramatically simplifying the device fabrication processes and suitable for metrology applications [79]. This is ascribed to the higher photoconductive gain and detectivity in our devices. Therefore, it would be interesting to see the effect of electrostatic gating in the charge transfer process. Further studies on the photoresponses of gate-free devices are called for in *p-n* junctions devices [77,78] on the millimeter scale.

4. Conclusions

In summary, we have fabricated binary photodetector devices using epitaxial graphene on SiC substrates. The binary photoresponse mainly originates from the energy band alignment of the IBL/EG interface and the highly sensitive work function of the graphene layer. In the case of 405–532 nm laser illumination, the photocurrent is dominated by resultant *n* doping in the graphene layer due to the combined effect of photo-absorption both in IBL and EG, as well as the release of physisorbed molecule from the EG layer. On the other hand, in the case of 632–980 nm, the absorption in the EG produce photo-excited electrons, which relax to the IBL layer in the ultrafast time domain, resulting in a negative photocurrent. The highest photoresponsivity of the device is > 10 A/W, which is higher than the required photoresponsivity of 1 A/W for practical applications [12]. The obtained detectivity is as high as 10^7 Jones.

Table 2
A comparison of the photodetector performances of our device with earlier reported graphene on SiC-based photodetectors.

Materials	Wavelength (nm)	V_{DS} (V)	Max. R (A/W)	Gate Voltage (V)	Photoresponse (Nature)	Ref.
EG/4H–SiC	405–980	1	>10	0	Binary	This Work
Graphene/4H–SiC	325	−3	254.1	±3	Binary	[44]
Graphene/SiC	400	−0.5	7.4	±20	Binary	[75]
Graphene/SiC	≤413	–	–	±20	Binary	[41]
Graphene/SiC	532	0.75	18	−30	Single	[38]
Graphene/4H–SiC	254–365	5	0.009	0	Single	[36]
Graphene/4H–SiC	650	10	5.11	0	Single	[37]
EG/SiC SEPT	365	30	1.2	0	Single	[76]

We believe that our results call for further theoretical investigations to provide in depth insight into the system. It would be fascinating to explore the effect of electrostatic gating to the interlayer transport of the photocarriers. Additionally, metals intercalation between EG and SiC systems may dramatically influence the optoelectronic and magneto-optical properties of the system, which worth investigating. The unique photoinduced dual charge transfer phenomenon in EG on 4H–SiC implies that the electron density of EG can be adjusted by photon energy, which is promising in metrology applications, such as UV photometry.

CRediT authorship contribution statement

Shivi Rathore: Formal analysis, Writing – original draft, designed the experiment and collected and analyzed data. The manuscript was written with contributions from all authors. **Dinesh Kumar Patel:** Formal analysis, Writing – original draft, designed the experiment and collected and analyzed data. grew the graphene and fabricated the devices. The manuscript was written with contributions from all authors. **Mukesh Kumar Thakur:** Formal analysis, Writing – original draft, designed the experiment and collected and analyzed data. The manuscript was written with contributions from all authors. **Golam Haider:** Formal analysis, Writing – original draft, analyzed data and provided manuscript oversight. The manuscript was written with contributions from all authors. **Martin Kalbac:** Formal analysis, Writing – original draft, analyzed data and provided manuscript oversight. The manuscript was written with contributions from all authors. **Mattias Kruskopf:** Writing – original draft, grew the graphene and fabricated the devices. The manuscript was written with contributions from all authors. **Chieh-I Liu:** Writing – original draft, grew the graphene and fabricated the devices. The manuscript was written with contributions from all authors. **Albert F. Rigosi:** Writing – original draft, provided general project oversight and guidance. The manuscript was written with contributions from all authors. **Randolph E. Elmquist:** Writing – original draft, provided general project oversight and guidance. The manuscript was written with contributions from all authors. **Chi-Te Liang:** Writing – original draft, provided general project oversight and guidance. The manuscript was written with contributions from all authors. **Po-Da Hong:** Writing – original draft, provided general project oversight and guidance. The manuscript was written with contributions from all authors. The authors would like to express thanks to S Payagala and A Levy for their assistance in the NIST internal review process.

Declaration of competing interest

The authors declare that they have no known competing financial interests or personal relationships that could have appeared to influence the work reported in this paper.

Acknowledgments

This work was partially funded by the Ministry of Science and Technology (MOST), Taiwan. S.R. and P.D.H. acknowledge financial support from MOST (grant number MOST 109-2221-E-011-161-MY3). D.K.P. acknowledges financial support from MOST (grant number MOST 109-2811-M-002-639). M.K.T., G.H., and M.K. greatly acknowledge support from Czech Science Foundation, Czechia, project No. 20–08633X. The authors would like to express thanks to S Payagala and A Levy for their assistance in the NIST internal review process.

Commercial equipment, instruments, and materials are identified in this paper in order to specify the experimental procedure adequately. Such identification is not intended to imply recommendation or endorsement by the National Institute of Standards and Technology or the United States government, nor is it intended to imply that the materials

or equipment identified are necessarily the best available for the purpose.

Appendix A. Supplementary data

Supplementary data to this article can be found online at https://doi.org/10.1016/j.carbon.2021.07.098.

References

[1] M.K. Thakur, A. Gupta, S. Ghosh, S. Chattopadhyay, Graphene-conjugated upconversion nanoparticles as fluorescence-tuned photothermal nanoheaters for desalination, ACS Applied Nano Materials 2 (4) (2019) 2250–2259.

[2] F. Xia, T. Mueller, Y.-M. Lin, A. Valdes-Garcia, P. Avouris, Ultrafast graphene photodetector, Nat. Nanotechnol. 4 (12) (2009) 839–843.

[3] T. Mueller, F. Xia, P. Avouris, Graphene photodetectors for high-speed optical communications, Nat. Photonics 4 (5) (2010) 297–301.

[4] L. Banszerus, M. Schmitz, S. Engels, J. Dauber, M. Oellers, F. Haupt, K. Watanabe, T. Taniguchi, B. Beschoten, C. Stampfer, Ultrahigh-mobility graphene devices from chemical vapor deposition on reusable copper, Science Advances 1 (6) (2015) e1500222.

[5] P. Avouris, Z. Chen, V. Perebeinos, Carbon-based electronics, Nat. Nanotechnol. 2 (10) (2007) 605–615.

[6] K.I. Bolotin, K.J. Sikes, Z. Jiang, M. Klima, G. Fudenberg, J. Hone, P. Kim, H.L. Stormer, Ultrahigh electron mobility in suspended graphene, Solid State Commun. 146 (9) (2008) 351–355.

[7] A.K. Geim, K.S. Novoselov, The rise of graphene, Nat. Mater. 6 (3) (2007) 183–191.

[8] K.S. Novoselov, V.I. Fal′ko, L. Colombo, P.R. Gellert, M.G. Schwab, K. Kim, A roadmap for graphene, Nature 490 (7419) (2012) 192–200.

[9] R.R. Nair, P. Blake, A.N. Grigorenko, K.S. Novoselov, T.J. Booth, T. Stauber, N.M.R. Peres, A.K. Geim, Fine structure constant defines visual transparency of graphene, Science 320 (5881) (2008) 1308-1308.

[10] F.H.L. Koppens, T. Mueller, P. Avouris, A.C. Ferrari, M.S. Vitiello, M. Polini, Photodetectors based on graphene, other two-dimensional materials and hybrid systems, Nat. Nanotechnol. 9 (10) (2014) 780–793.

[11] M. Freitag, T. Low, F. Xia, P. Avouris, Photoconductivity of biased graphene, Nat. Photonics 7 (1) (2013) 53–59.

[12] C.-H. Liu, Y.-C. Chang, T.B. Norris, Z. Zhong, Graphene photodetectors with ultra-broadband and high responsivity at room temperature, Nat. Nanotechnol. 9 (4) (2014) 273–278.

[13] L. Vicarelli, M.S. Vitiello, D. Coquillat, A. Lombardo, A.C. Ferrari, W. Knap, M. Polini, V. Pellegrini, A. Tredicucci, Graphene field-effect transistors as room-temperature terahertz detectors, Nat. Mater. 11 (10) (2012) 865–871.

[14] G. Konstantatos, M. Badioli, L. Gaudreau, J. Osmond, M. Bernechea, F.P.G. de Arquer, F. Gatti, F.H.L. Koppens, Hybrid graphene–quantum dot phototransistors with ultrahigh gain, Nat. Nanotechnol. 7 (6) (2012) 363–368.

[15] N.M. Gabor, J.C.W. Song, Q. Ma, N.L. Nair, T. Taychatanapat, K. Watanabe, T. Taniguchi, L.S. Levitov, P. Jarillo-Herrero, Hot carrier–assisted intrinsic photoresponse in graphene, Science 334 (6056) (2011) 648–652.

[16] T.J. Echtermeyer, P.S. Nene, M. Trushin, R.V. Gorbachev, A.L. Eiden, S. Milana, Z. Sun, J. Schliemann, E. Lidorikis, K.S. Novoselov, A.C. Ferrari, Photothermoelectric and photoelectric contributions to light detection in metal–graphene–metal photodetectors, Nano Lett. 14 (7) (2014) 3733–3742.

[17] M.H. Kim, J. Yan, R.J. Suess, T.E. Murphy, M.S. Fuhrer, H.D. Drew, Photothermal response in dual-gated bilayer graphene, Phys. Rev. Lett. 110 (24) (2013) 247402.

[18] J. Chen, J. Xu, S. Shi, R. Cao, D. Liu, Y. Bu, P. Yang, J. Xu, X. Zhang, L. Li, Novel self-powered photodetector with binary photoswitching based on SnSx/TiO2 heterojunctions, ACS Appl. Mater. Interfaces 12 (20) (2020) 23145–23154.

[19] K. Yan, D. Wu, H. Peng, L. Jin, Q. Fu, X. Bao, Z. Liu, Modulation-doped growth of mosaic graphene with single-crystalline p–n junctions for efficient photocurrent generation, Nat. Commun. 3 (1) (2012) 1280.

[20] F. Larki, Y. Abdi, P. Kameli, H. Salamati, An effort towards full graphene photodetectors, Photonic Sensors (2020).

[21] M.K. Thakur, C.-Y. Fang, Y.-T. Yang, T.A. Effendi, P.K. Roy, R.-S. Chen, K.K. Ostrikov, W.-H. Chiang, S. Chattopadhyay, Microplasma-enabled graphene quantum dot-wrapped gold nanoparticles with synergistic enhancement for broad band photodetection, ACS Appl. Mater. Interfaces 12 (25) (2020) 28550–28560.

[22] A. Gupta, M.K. Thakur, T.A. Effendi, R.-S. Chen, H.-Y. Cheng, K.-H. Lin, M. Bouras, D.S. Tomar, H.Y. Kuo, S. Chattopadhyay, Metallo-graphene enhanced upconversion luminescence for broadband photodetection under polychromatic illumination, Chem. Eng. J. (2020) 127608.

[23] D. Sun, G. Aivazian, A.M. Jones, J.S. Ross, W. Yao, D. Cobden, X. Xu, Ultrafast hot-carrier-dominated photocurrent in graphene, Nat. Nanotechnol. 7 (2) (2012) 114–118.

[24] A. Urich, K. Unterrainer, T. Mueller, Intrinsic response time of graphene photodetectors, Nano Lett. 11 (7) (2011) 2804–2808.

[25] S.Y. Zhou, G.H. Gweon, A.V. Fedorov, P.N. First, W.A. de Heer, D.H. Lee, F. Guinea, A.H. Castro Neto, A. Lanzara, Substrate-induced bandgap opening in epitaxial graphene, Nat. Mater. 6 (10) (2007) 770–775.

[26] X. Peng, R. Ahuja, Symmetry breaking induced bandgap in epitaxial graphene layers on SiC, Nano Lett. 8 (12) (2008) 4464–4468.

[27] C. Yu, J. Li, Q.B. Liu, S.B. Dun, Z.Z. He, X.W. Zhang, S.J. Cai, Z.H. Feng, Buffer layer induced band gap and surface low energy optical phonon scattering in epitaxial graphene on SiC(0001), Appl. Phys. Lett. 102 (1) (2013) 013107.

[28] A.F. Rigosi, H.M. Hill, N.R. Glavin, S.J. Pookpanratana, Y. Yang, A.G. Boosalis, J. Hu, A. Rice, A.A. Allerman, N.V. Nguyen, C.A. Hacker, R.E. Elmquist, A.R. Hight Walker, D.B. Newell, Measuring the dielectric and optical response of millimeter-scale amorphous and hexagonal boron nitride films grown on epitaxial graphene, 2D Materials 5 (2018) 11011-1-011011–10, https://doi.org/10.1088/2053-1583/aa9ea3.

[29] M.S. Nevius, M. Conrad, F. Wang, A. Celis, M.N. Nair, A. Taleb-Ibrahimi, A. Tejeda, E.H. Conrad, Semiconducting graphene from highly ordered substrate interactions, Phys. Rev. Lett. 115 (13) (2015) 136802.

[30] H.M. Hill, A.F. Rigosi, S. Chowdhury, Y. Yang, N. Nguyen, F. Tavazza, R.E. Elmquist, D.B. Newell, A.R. Hight Walker, Probing the dielectric response of the interfacial buffer layer in epitaxial graphene via optical spectroscopy, Phys. Rev. B 96 (2017) 195437.

[31] I. Shtepliuk, T. Iakimov, V. Khranovskyy, J. Eriksson, F. Giannazzo, R. Yakimova, Role of the potential barrier in the electrical performance of the graphene/SiC interface, Crystals 7 (6) (2017) 162.

[32] A.R. Panna, I.F. Hu, M. Kruskopf, D.K. Patel, D.G. Jarrett, C.-I. Liu, S.U. Payagala, D. Saha, A.F. Rigosi, D.B. Newell, C.-T. Liang, R.E. Elmquist, Graphene quantum Hall effect parallel resistance arrays, Phys. Rev. B 103 (7) (2021) 075408.

[33] R.S. Singh, D. Li, Q. Xiong, I. Santoso, X. Yu, W. Chen, A. Rusydi, A.T.S. Wee, Anomalous photoresponse in the deep-ultraviolet due to resonant excitonic effects in oxygen plasma treated few-layer graphene, Carbon 106 (2016) 330–335.

[34] H. Bencherif, L. Dehimi, G. Messina, P. Vincent, F. Pezzimenti, F.G.D. Corte, An optimized Graphene/4H-SiC/Graphene MSM UV-photodetector operating in a wide range of temperature, Sensor Actuator Phys. 307 (2020) 112007.

[35] J. Yang, L. Guo, Y. Guo, W. Hu, Z. Zhang, Epitaxial graphene/SiC Schottky ultraviolet photodiode with orders of magnitude adjustability in responsivity and response speed, Appl. Phys. Lett. 112 (10) (2018) 103501.

[36] E. Kus demir, D. Özkendir, V. Fırat, C. Çelebi, Epitaxial graphene contact electrode for silicon carbide based ultraviolet photodetector, J. Phys. Appl. Phys. 48 (9) (2015) 095104.

[37] X. Li, X. Chen, X. Xu, X. Hu, Z. Zuo, Enhanced performance of a visible light detector made with quasi-free-standing graphene on SiC, Materials 12 (19) (2019) 3227.

[38] B.K. Sarker, E. Cazalas, T.-F. Chung, I. Childres, I. Jovanovic, Y.P. Chen, Position-dependent and millimetre-range photodetection in phototransistors with micrometre-scale graphene on SiC, Nat. Nanotechnol. 12 (7) (2017) 668–674.

[39] N.Z. Butt, B.K. Sarker, Y.P. Chen, M.A. Alam, Substrate-induced photofield effect in graphene phototransistors, IEEE Trans. Electron. Dev. 62 (11) (2015) 3734–3741.

[40] S. Sonde, F. Giannazzo, V. Raineri, R. Yakimova, J.R. Huntzinger, A. Tiberj, J. Camassel, Electrical properties of the graphene/$4H\text{-SiC}$ (0001) interface probed by scanning current spectroscopy, Phys. Rev. B 80 (24) (2009) 241406.

[41] E. Cazalas, I. Childres, A. Majcher, T.-F. Chung, Y.P. Chen, I. Jovanovic, Hysteretic response of chemical vapor deposition graphene field effect transistors on SiC substrates, Appl. Phys. Lett. 103 (5) (2013) 053123.

[42] R. Sun, Y. Zhang, K. Li, C. Hui, K. He, X. Ma, F. Liu, Tunable photoresponse of epitaxial graphene on SiC, Appl. Phys. Lett. 103 (1) (2013) 013106.

[43] J. Huang, L.-W. Guo, W. Lu, Y.-H. Zhang, Z. Shi, Y.-P. Jia, Z.-L. Li, J.-W. Yang, H.-X. Chen, Z.-X. Mei, X.-L. Chen, A self-powered sensitive ultraviolet photodetector based on epitaxial graphene on silicon carbide, Chin. Phys. B 25 (6) (2016) 067205.

[44] Y. Li, P. Chen, X. Chen, R. Xu, M. Liu, J. Zhou, C. Ge, H. Peng, X. Mao, J. Feng, X. Hu, Y. Peng, X. Xu, Z. Xie, X. Xiu, D. Chen, B. Liu, P. Han, Y. Shi, R. Zhang, Y. Zheng, High-responsivity graphene/4H-SiC ultraviolet photodetector based on a planar junction formed by the dual modulation of electric and light fields, Advanced optical materials 8 (19) (2020) 2000559.

[45] J.A. Alexander-Webber, A.M.R. Baker, T.J.B.M. Janssen, A. Tzalenchuk, S. Lara-Avila, S. Kubatkin, R. Yakimova, B.A. Piot, D.K. Maude, R.J. Nicholas, Phase space for the breakdown of the quantum Hall effect in epitaxial graphene, Phys. Rev. Lett. 111 (9) (2013).

[46] J.A. Alexander-Webber, J. Huang, D.K. Maude, T.J.B.M. Janssen, A. Tzalenchuk, V. Antonov, T. Yager, S. Lara-Avila, S. Kubatkin, R. Yakimova, R.J. Nicholas, Giant quantum Hall plateaus generated by charge transfer in epitaxial graphene, Sci Rep-Uk 6 (2016).

[47] M. Kruskopf, R.E. Elmquist, Epitaxial graphene for quantum resistance metrology, Metrologia 55 (4) (2018) R27–R36.

[48] D.K. Patel, Quantum Hall Effect in Millimeter-Scale, Mono-Layer Epitaxial Graphene P-N Junctions, Department of Physics, National Taiwan University, AiritiLibrary, 2020, pp. 1–137.

[49] M. Kruskopf, D.M. Pakdehi, K. Pierz, S. Wundrack, R. Stosch, T. Dziomba, M. Götz, J. Baringhaus, J. Aprojanz, C. Tegenkamp, J. Lidzba, T. Seyller, F. Hohls, F.J. Ahlers, H.W. Schumacher, Comeback of epitaxial graphene for electronics: large-area growth of bilayer-free graphene on SiC, 2D Mater. 3 (4) (2016) 041002.

[50] Y. Yang, L.-I. Huang, Y. Fukuyama, F.-H. Liu, M.A. Real, P. Barbara, C.-T. Liang, D.B. Newell, R.E. Elmquist, Low Carrier Density Epitaxial Graphene Devices On SiC 11 (1) (2015) 90–95.

[51] C. Riedl, C. Coletti, U. Starke, Structural and electronic properties of epitaxial graphene on SiC(0 0 0 1): a review of growth, characterization, transfer doping and hydrogen intercalation, J. Phys. Appl. Phys. 43 (37) (2010) 374009.

[52] U. Starke, J. Schardt, J. Bernhardt, M. Franke, K. Heinz, Stacking transformation from hexagonal to cubic SiC induced by surface reconstruction: a seed for heterostructure growth, Phys. Rev. Lett. 82 (10) (1999) 2107–2110.

[53] M. Kruskopf, A.F. Rigosi, A.R. Panna, M. Marzano, D. Patel, H. Jin, D.B. Newell, R.E. Elmquist, Next-generation crossover-free quantum Hall arrays with superconducting interconnections, Metrologia 56 (6) (2019).

[54] M. Kruskopf, A.F. Rigosi, A.R. Panna, D.K. Patel, H. Jin, M. Marzano, M. Berilla, D.B. Newell, R.E. Elmquist, Two-terminal and multi-terminal designs for next-generation

quantized Hall resistance standards: contact material and geometry, IEEE Trans. Electron. Dev. 66 (9) (2019) 3973–3977.
[55] C.-Y. Wang, Y.-W. Lin, C. Chuang, C.-H. Yang, D.K. Patel, S.-Z. Chen, C.-C. Yeh, W.-C. Chen, C.-C. Lin, Y.-H. Chen, W.-H. Wang, R. Sankar, F.-C. Chou, M. Kruskopf, R.E. Elmquist, C.-T. Liang, Magnetotransport in hybrid InSe/monolayer graphene on SiC, Nanotechnology 32 (15) (2021) 155704.
[56] Z.H. Ni, W. Chen, X.F. Fan, J.L. Kuo, T. Yu, A.T.S. Wee, Z.X. Shen, Raman spectroscopy of epitaxial graphene on a SiC substrate, Phys. Rev. B 77 (11) (2008) 115416.
[57] S.-H. Bae, X. Zhou, S. Kim, Y.S. Lee, S.S. Cruz, Y. Kim, J.B. Hannon, Y. Yang, D.K. Sadana, F.M. Ross, H. Park, J. Kim, Unveiling the carrier transport mechanism in epitaxial graphene for forming wafer-scale, single-domain graphene, Proc. Natl. Acad. Sci. Unit. States Am. 114 (16) (2017) 4082–4086.
[58] V. Panchal, Y. Yang, G. Cheng, J. Hu, M. Kruskopf, C.-I. Liu, A.F. Rigosi, C. Melios, A.R. Hight Walker, D.B. Newell, O. Kazakova, R.E. Elmquist, Confocal laser scanning microscopy for rapid optical characterization of graphene, Commun. Phys. 1 (1) (2018) 83.
[59] G. Haider, P. Roy, C.-W. Chiang, W.-C. Tan, Y.-R. Liou, H.-T. Chang, C.-T. Liang, W.-H. Shih, Y.-F. Chen, Electrical-polarization-induced ultrahigh responsivity photodetectors based on graphene and graphene quantum dots, Adv. Funct. Mater. 26 (4) (2016) 620–628.
[60] G. Haider, R. Ravindranath, T.-P. Chen, P. Roy, P.K. Roy, S.-Y. Cai, H.-T. Chang, Y.-F. Chen, Dirac point induced ultralow-threshold laser and giant optoelectronic quantum oscillations in graphene-based heterojunctions, Nat. Commun. 8 (1) (2017) 256.
[61] K.P. Bera, G. Haider, M. Usman, P.K. Roy, H.-I. Lin, Y.-M. Liao, C.R.P. Inbaraj, Y.-R. Liou, M. Kataria, K.-L. Lu, Y.-F. Chen, Trapped photons induced ultrahigh external quantum efficiency and photoresponsivity in hybrid graphene/metal-organic framework broadband wearable photodetectors, Adv. Funct. Mater. 28 (51) (2018) 1804802.
[62] K.P. Bera, G. Haider, Y.-T. Huang, P.K. Roy, C.R. Paul Inbaraj, Y.-M. Liao, H.-I. Lin, C.-H. Lu, C. Shen, W.Y. Shih, W.-H. Shih, Y.-F. Chen, Graphene sandwich stable perovskite quantum-dot light-emissive ultrasensitive and ultrafast broadband vertical phototransistors, ACS Nano 13 (11) (2019) 12540–12552.
[63] C. Heide, M. Hauck, T. Higuchi, J. Ristein, L. Ley, H.B. Weber, P. Hommelhoff, Attosecond-fast internal photoemission, Nat. Photonics 14 (4) (2020) 219–222.
[64] A.F. Rigosi, N.R. Glavin, C.-I. Liu, Y. Yang, J. Obrzut, H.M. Hill, J. Hu, H.-Y. Lee, A.R. Hight Walker, C.A. Richter, R.E. Elmquist, D.B. Newell, Preservation of surface conductivity and dielectric loss tangent in large-scale, encapsulated epitaxial graphene measured by noncontact microwave cavity perturbations, Small 13 (26) (2017) 1700452.
[65] Z. Li, Y. Wang, A. Kozbial, G. Shenoy, F. Zhou, R. McGinley, P. Ireland, B. Morganstein, A. Kunkel, S.P. Surwade, L. Li, H. Liu, Effect of airborne contaminants on the wettability of supported graphene and graphite, Nat. Mater. 12 (10) (2013) 925–931.
[66] A. Kozbial, F. Zhou, Z. Li, H. Liu, L. Li, Are graphitic surfaces hydrophobic?, Accounts Chem. Res. 49 (12) (2016) 2765–2773.
[67] G. Haider, Y.-H. Wang, F.J. Sonia, C.-W. Chiang, O. Frank, J. Vejpravova, M. Kalbáč, Y.-F. Chen, Rippled metallic-nanowire/graphene/semiconductor nanostack for a gate-tunable ultrahigh-performance stretchable phototransistor, Advanced Optical Materials 8 (19) (2020) 2000859.
[68] W. Yuan, G. Shi, Graphene-based gas sensors, J. Mater. Chem. 1 (35) (2013) 10078–10091.
[69] T.L. Sun, T. Kurokawa, S. Kuroda, A.B. Ihsan, T. Akasaki, K. Sato, M.A. Haque, T. Nakajima, J.P. Gong, Physical hydrogels composed of polyampholytes demonstrate high toughness and viscoelasticity, Nat. Mater. 12 (10) (2013) 932–937.
[70] C.J. Docherty, C.-T. Lin, H.J. Joyce, R.J. Nicholas, L.M. Herz, L.-J. Li, M.B. Johnston, Extreme sensitivity of graphene photoconductivity to environmental gases, Nat. Commun. 3 (1) (2012) 1228.
[71] M.Z. Iqbal, S. Siddique, A. Khan, D. Sung, J. Eom, S. Hong, Ultraviolet-light-driven charge carriers tunability mechanism in graphene, Mater. Des. 159 (2018) 232–239.
[72] Y. Zhao, Y. Qiu, J. Feng, J. Zhao, G. Chen, H. Gao, Y. Zhao, L. Jiang, Y. Wu, Chiral 2D-perovskite nanowires for Stokes photodetectors, J. Am. Chem. Soc. 143 (22) (2021) 8437–8445.
[73] M.K. Thakur, A. Gupta, M.Y. Fakhri, R.S. Chen, C.T. Wu, K.H. Lin, S. Chattopadhyay, Optically coupled engineered upconversion nanoparticles and graphene for a high responsivity broadband photodetector, Nanoscale 11 (19) (2019) 9716–9725.
[74] Z. Liu, H. Huang, B. Liang, X. Wang, Z. Wang, D. Chen, G. Shen, Zn2GeO4 and In2Ge2O7 nanowire mats based ultraviolet photodetectors on rigid and flexible substrates, Opt Express 20 (3) (2012) 2982–2991.
[75] I.C.B.K. Sarker, E. Cazalas, I. Jovanovic, Y.P. Chen, Gate-tunable and High Responsivity Graphene Phototransistors on Undoped Semiconductor Substrates, 2015 arXiv.
[76] V.S.N. Chava, B.G. BarkerJr, A. Balachandran, A. Khan, G. Simin, A.B. Greytak, M.V. S. Chandrashekhar, High detectivity visible-blind SiF4 grown epitaxial graphene/SiC Schottky contact bipolar phototransistor, Appl. Phys. Lett. 111 (24) (2017) 243504.
[77] A.F. Rigosi, D. Patel, M. Marzano, M. Kruskopf, H.M. Hill, H. Jin, J. Hu, A.R. Hight Walker, M. Ortolano, L. Callegaro, C.-T. Liang, D.B. Newell, Atypical quantized resistances in millimeter-scale epitaxial graphene p-n junctions, Carbon 154 (2019) 230–237.
[78] D. Patel, M. Marzano, C.-I. Liu, H.M. Hill, M. Kruskopf, H. Jin, J. Hu, D.B. Newell, C.-T. Liang, R. Elmquist, A.F. Rigosi, Accessing ratios of quantized resistances in graphene p–n junction devices using multiple terminals, AIP Adv. 10 (2) (2020) 025112.
[79] A.F. Rigosi, R.E. Elmquist, The quantum Hall effect in the era of the new SI, Semicond. Sci. Technol. 34 (2019) 93004-1-093004–093009, https://doi.org/10.1088/1361-6641/ab37d3.